MARTIN MARIETTA ENERGY SYSTEMS LIBRARIES

3 4456 0354614 3

ORNL/TM-11737

ornl

OAK RIDGE
NATIONAL
LABORATORY

MARTIN MARIETTA

Z_{eff} Measurements in ATF Using Visible Bremsstrahlung

S. Morita
R. K. Richards
L. D. Horton
R. C. Isler
E. C. Crume, Jr.
M. Murakami

OAK RIDGE NATIONAL LABORATORY
CENTRAL RESEARCH LIBRARY
CIRCULATION SECTION
4500N ROOM 175
LIBRARY LOAN COPY
DO NOT TRANSFER TO ANOTHER PERSON
If you wish someone else to see this report, send in name with report and the library will arrange a loan.

MANAGED BY
MARTIN MARIETTA ENERGY SYSTEMS, INC.
FOR THE UNITED STATES
DEPARTMENT OF ENERGY

This report has been reproduced directly from the best available copy.

Available to DOE and DOE contractors from the Office of Scientific and Technical Information, P.O. Box 62, Oak Ridge, TN 37831; prices available from (615) 576-8401, FTS 626-8401.

Available to the public from the National Technical Information Service, U.S. Department of Commerce, 5285 Port Royal Rd., Springfield, VA 22161.

This report was prepared as an account of work sponsored by an agency of the United States Government. Neither the United States Government nor any agency thereof, nor any of their employees, makes any warranty, express or implied, or assumes any legal liability or responsibility for the accuracy, completeness, or usefulness of any information, apparatus, product, or process disclosed, or represents that its use would not infringe privately owned rights. Reference herein to any specific commercial product, process, or service by trade name, trademark, manufacturer, or otherwise, does not necessarily constitute or imply its endorsement, recommendation, or favoring by the United States Government or any agency thereof. The views and opinions of authors expressed herein do not necessarily state or reflect those of the United States Government or any agency thereof.

ORNL/TM-11737
Dist. Category UC-426

Fusion Energy Division

Z_{eff} MEASUREMENTS IN ATF USING VISIBLE BREMSSTRAHLUNG

S. Morita
National Institute for Fusion Science, Nagoya, Japan

R. K. Richards
L. D. Horton
R. C. Isler
E. C. Crume, Jr.
M. Murakami

Date published: April 1991

Prepared for the
Office of Fusion Energy
Budget Activity No. AT 10 10 15 B

Prepared by the
OAK RIDGE NATIONAL LABORATORY
Oak Ridge, Tennessee 37831-6285
managed by
MARTIN MARIETTA ENERGY SYSTEMS, INC.
for the
U.S. DEPARTMENT OF ENERGY
under contract DE-AC05-84OR21400

MARTIN MARIETTA ENERGY SYSTEMS LIBRARIES
3 4456 0354614 3

CONTENTS

ABSTRACT v
1. INTRODUCTION 1
2. CALCULATION OF Z_{eff} AND TREATMENT OF THE TEMPERATURE DEPENDENCE 2
3. EXPERIMENTAL APPARATUS 4
4. EXPERIMENTAL RESULTS AND DISCUSSION 12
5. SUMMARY 20
ACKNOWLEDGMENT 24
REFERENCES 25

ABSTRACT

Measurements of the effective charge Z_{eff} in plasmas with electron cyclotron heating (ECH) and neutral beam injection (NBI) in the Advanced Toroidal Facility (ATF) have been carried out using visible bremsstrahlung. The electron temperature needed for the analysis is calculated from the measured stored energy and electron density. The value of Z_{eff} varies widely depending on experimental conditions. In ECH plasmas it is between 2 and 8. In NBI plasmas, which are subject to radiation collapse, Z_{eff} is between 3 and 5 at the time the stored energy reaches a maximum. However, Z_{eff} is less than 2.5 in quasi-steady medium-density plasmas and is close to 1.2 in the highest-density plasmas, where the average electron density $\overline{n}_e$ is of the order of 10^{14} cm^{-3}.

1. INTRODUCTION

An investigation of impurity behavior is an important aspect of studies of magnetically confined plasmas. An understanding of impurity behavior is particularly needed during auxiliary heating with neutral beam injection (NBI) or with ion cyclotron heating (ICH) when plasma-material interactions can be strong, since density limits and confinement times may be restricted by impurity radiation from sputtered contaminants. Also, it is important to understand impurity behavior in order to control it in reactors, where dilution of the deuterium and tritium fuel could reduce the fusion energy output. Impurity problems may be more severe in helical devices than in tokamaks because plasma-wall interaction can be intense near the coil grooves that protrude into the vacuum chamber of a helical device, even if an internal separatrix exists in the magnetic configuration. However, in contrast to tokamaks, few investigations of impurity behavior have been performed in helical devices [1–3], and more extensive studies are needed.

The effective charge Z_{eff} is a convenient measure of impurity levels, although the specific composition of impurities cannot be determined from this parameter. A number of measurements have been exploited to evaluate Z_{eff} in fusion studies: visible bremsstrahlung, plasma resistivity, soft X rays, and neutron yields. Plasma resistivity measurements cannot be used in helical devices such as the Advanced Toroidal Facility (ATF), which have no imposed toroidal current. The analysis of soft X-ray continua tends to be complicated because some assumptions must be made about the impurity composition in order to evaluate densities from the recombination radiation that dominates the spectrum. The neutron yield is very sensitive to the ion temperatures, so determinations of Z_{eff} from this type of measurement have large uncertainties. Visible bremsstrahlung provides the best data for making Z_{eff} measurements because the analysis is relatively straightforward [4,5].

NBI heating is used extensively in helical devices. However, the stored energy frequently exhibits a collapse because of falling electron temperature and a concomitant growth of impurity radiation [6,7]. In order to reduce the level of low-Z radiation and to gain better control over the plasma density, gettering with chromium and with titanium was implemented in ATF. After titanium gettering, it was possible to obtain quasi-steady NBI plasmas in the high-density regime ($\overline{n}_e \approx 10^{14}$ cm^{-3}) [8], although low-density plasmas ($\overline{n}_e \leq 3 \times 10^{13}$ cm^{-3}) still collapsed. The results of Z_{eff} measurements after titanium gettering are summarized in this report, and the technical aspects of determining Z_{eff} from visible bremsstrahlung are discussed.

2. CALCULATION OF Z_{eff} AND TREATMENT OF THE TEMPERATURE DEPENDENCE

The bremsstrahlung (free-free) radiation from a single ion species in a plasma with a Maxwellian velocity distribution is given by [9]

$$\frac{\Delta P_{ff}}{\Delta\lambda} = \frac{16e^6}{3c^2}\left(\frac{\pi}{6m_e^3}\right)^{1/2}\frac{n_e n_i Z_i^2 \overline{g}_{ff}}{T_e^{1/2}\lambda^2}\exp\left(-\frac{hc}{T_e\lambda}\right), \tag{1}$$

where n_i is the density of ions in the charge state Z_i and $\overline{g}_{ff}$ is the free-free Gaunt factor. There is no free-bound continuum in the wavelength range used for the Z_{eff} measurements in ATF. Since magnetically confined plasmas generally include many kinds of impurities in various charge states, it is necessary to sum Eq. (1) over all ion species,

$$\epsilon_\lambda = \frac{\Delta P_{ff}}{\Delta\lambda} = \frac{(1.89\times10^{-28})n_e\sum_i n_i Z_i^2\overline{g}_{ff}}{T_e^{1/2}\lambda^2}\exp\left(-\frac{12400}{T_e\lambda}\right)\ [\text{W}\cdot\text{cm}^{-3}\cdot\text{Å}^{-1}], \tag{2}$$

where n_e and n_i are given in particles per cubic centimeter, T_e is given in electron volts, and λ is given in angstroms. The effective charge is defined by

$$Z_{\text{eff}} = \sum_i n_i Z_i^2 \Big/ \sum_i n_i Z_i = \sum_i n_i Z_i^2/n_e\ . \tag{3}$$

From Eqs. (2) and (3), Z_{eff} can be expressed as

$$Z_{\text{eff}} = \frac{\epsilon_\lambda T_e^{1/2}\lambda^2}{(1.89\times10^{-28})n_e^2\overline{g}_{ff}\exp(-12400/T\lambda)}\ . \tag{4}$$

The value of $\overline{g}_{ff}$ is given by Karzas and Latter [10]. It has the temperature dependence shown in Fig. 1 and can be approximated in the range between 0.1 keV and 2.0 keV by

$$\overline{g}_{ff} = 1.35T_e^{0.15}\ . \tag{5}$$

As a result, Z_{eff} as given by Eq. (4) has a temperature dependence of $T_e^{0.35}$, as illustrated in Fig. 2 [the exponential term containing T_e in Eq. (4) is essentially unity]. It is instructive to calculate Z_{eff} as a function of temperature for a fixed concentration of a single impurity. First we define the average charge $\overline{Q}$ as

$$\overline{Q} = \sum_i n_i Z_i \Big/ \sum_i n_i\ . \tag{6}$$

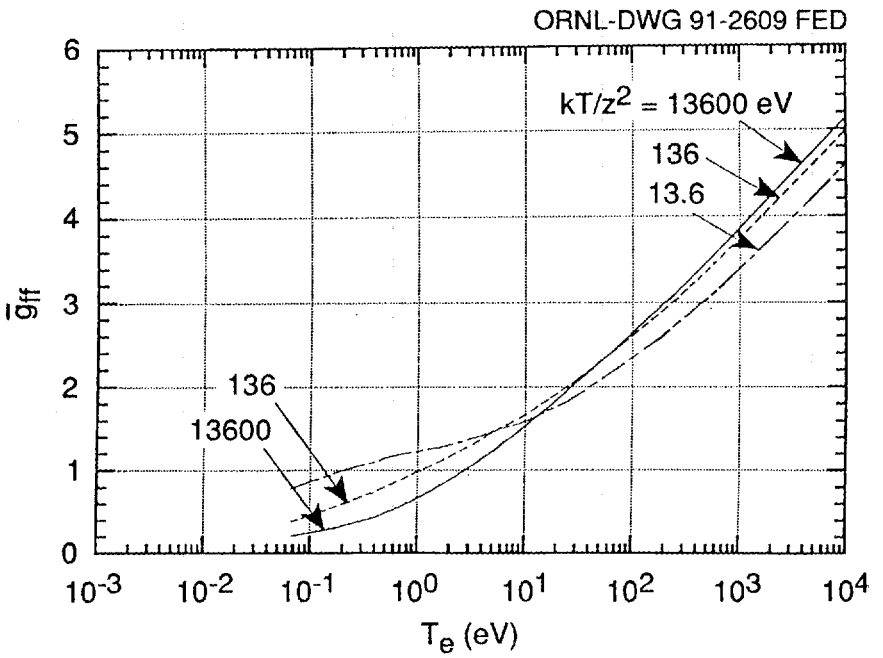

Fig. 1. Electron temperature dependence of temperature-averaged Gaunt factor $\overline{g}_{ff}$ as expressed by Karzas and Latter [10].

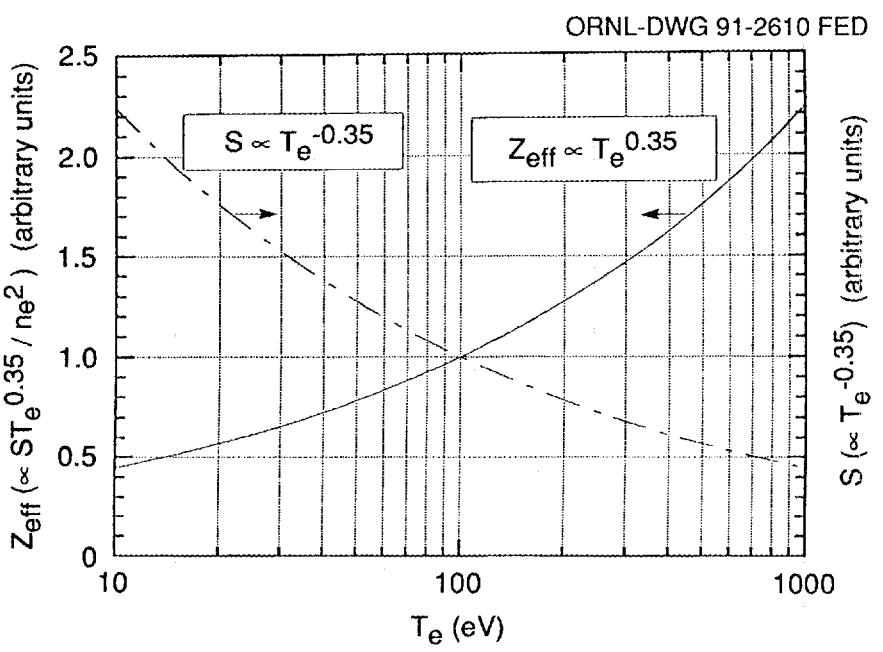

Fig. 2. Electron temperature dependence of visible bremsstrahlung and Z_{eff}.

Values of $\overline{Q}$ in the center of ATF plasmas (average minor radius $\overline{a}_p = 27$ cm) are shown in Fig. 3 for oxygen and in Fig. 4 for titanium. The calculations are made using an impurity transport code with a diffusion coefficient $D = 10^4$ cm^2/s and radial profiles $T_e(r) = T_{e0}[1-(r/a_p)^2]$ and $n_e(r) = n_{e0}[1-(r/a_p)^{30}]$. The value of $\overline{Q}$ does not change greatly in the range 0.1 keV $\leq T_e \leq$ 1 keV, because oxygen ions are easily ionized to the helium-like stage at $T_e = 0.1$ keV. However, $\overline{Q}$ monotonically increases as a function of temperature for titanium over the range indicated in Fig. 4. This dependence of $\overline{Q}$ on the electron temperature also means that the plasma $Z_{\rm eff}$ can be a strong function of temperature when titanium is the dominant impurity. The density dependence of $\overline{Q}$ is weak, as shown in Figs. 3 and 4. To obtain an idea of how $Z_{\rm eff}$ varies as a function of T_e, we investigate cases where impurity concentrations of 1% for both oxygen and titanium are assumed, i.e.,

$$\frac{\int_V n_{\rm imp}\, dV}{\int_V n_e\, dV} = 0.01 \ . \tag{7}$$

The results are shown in Figs. 5 and 6. For a 1% concentration of titanium alone, $Z_{\rm eff}$ is calculated to be 2.4 and 4.3 at electron temperatures of 0.2 keV and 1.0 keV, respectively, so that rapid changes of temperature as well as changes of concentration influence the visible bremsstrahlung measurement. If oxygen is assumed to be the only impurity, a 1% concentration produces a $Z_{\rm eff}$ of 1.38 for $T_e = 0.2$ keV and 1.60 for $T_e = 1.0$ keV.

3. EXPERIMENTAL APPARATUS

The instrumentation for the visible bremsstrahlung measurement consists of photodiodes and interference filters, which are coupled to a window on ATF with optical fibers. The photodiodes are EG&G Electro-Optics model TCN-1000-3 (an ultralow-noise photodiode and amplifier). The system is absolutely calibrated using a HeNe laser. The time constant of the system is 2 ms.

The optical fibers view the ATF plasma vertically with a spatial resolution of 38 mm$^\phi$ at a toroidal angle of 6°, as shown in Fig. 7. The line of sight for the single channel used in the present studies is a vertical chord at a major radius of 210 cm, the center of the ATF vacuum vessel. This line of sight also passes through the plasma center for low-β discharges with electron cyclotron heating (ECH), but the plasma center shifts outward 2–4 cm during NBI. The $Z_{\rm eff}$ measurements discussed here are not well localized but represent an average over a large fraction of the

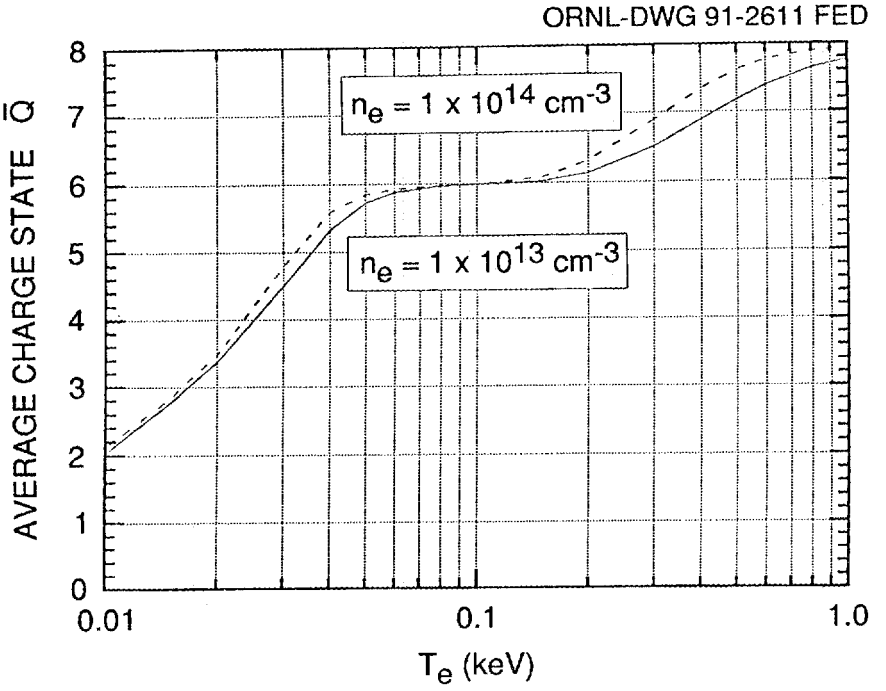

Fig. 3. Calculation of average charge state $\overline{Q}$ for oxygen at the plasma center as a function of electron temperature for $n_e = 1 \times 10^{13}$ cm^{-3} (solid line) and 1×10^{14} cm^{-3} (dashed line). A diffusion coefficient of $D = 10000$ cm^2/s and radial profiles of $T_e(r) = T_{e0}[1-(r/a_p)^2]$ and $n_e(r) = n_{e0}[1-(r/a_p)]^{30}$ are assumed in the calculations.

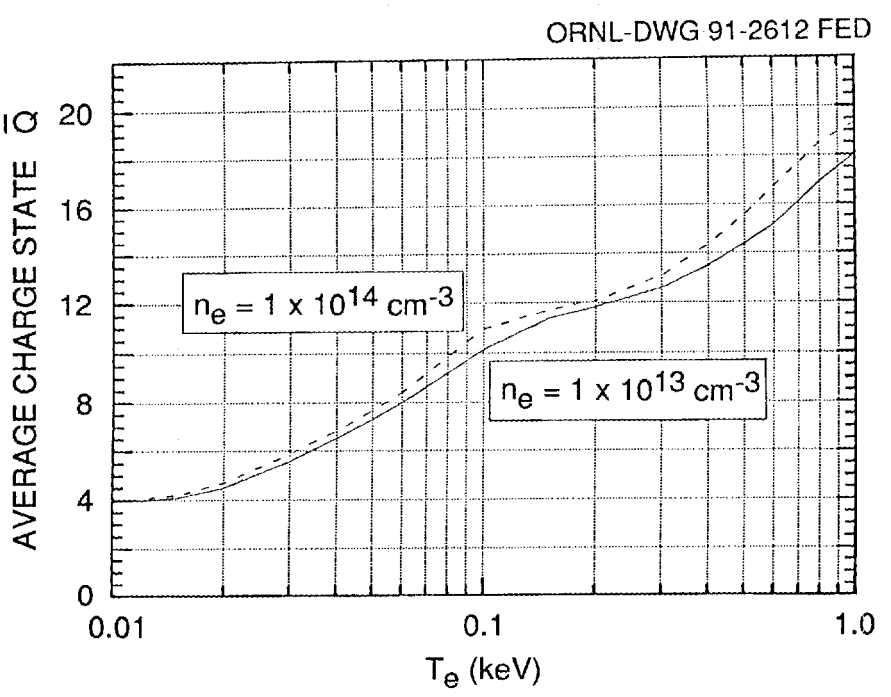

Fig. 4. Calculation of average charge state $\overline{Q}$ for titanium at the plasma center as a function of electron temperature for $n_e = 1 \times 10^{13}$ cm^{-3} (solid line) and 1×10^{14} cm^{-3} (dashed line).

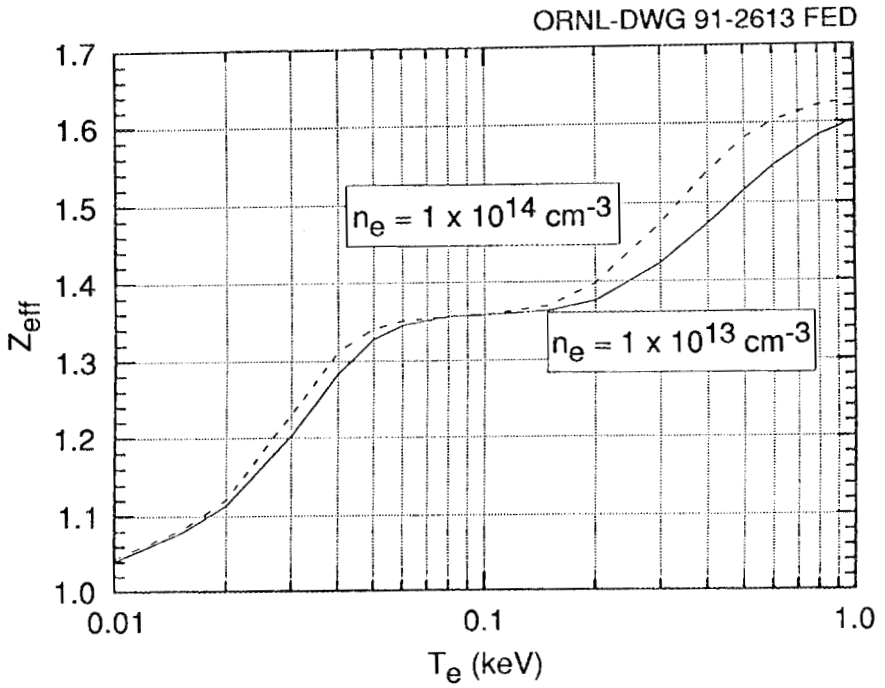

Fig. 5. Calculation of Z_{eff} for oxygen at the plasma center as a function of electron temperature for $n_e = 1 \times 10^{13}$ cm^{-3} (solid line) and 1×10^{14} cm^{-3} (dashed line). An oxygen fraction (n_{O}/n_e) of 1% is assumed in the calculation.

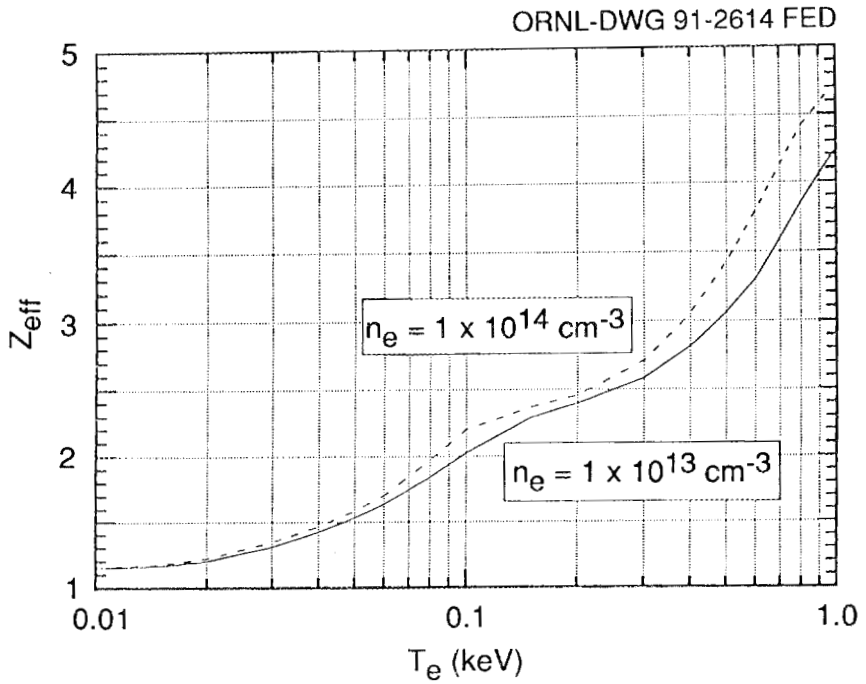

Fig. 6. Calculation of Z_{eff} for titanium at the plasma center as a function of electron temperature for $n_e = 1 \times 10^{13}$ cm^{-3} (solid line) and 1×10^{14} cm^{-3} (dashed line). A titanium fraction (n_{Ti}/n_e) of 1% is assumed in the calculation.

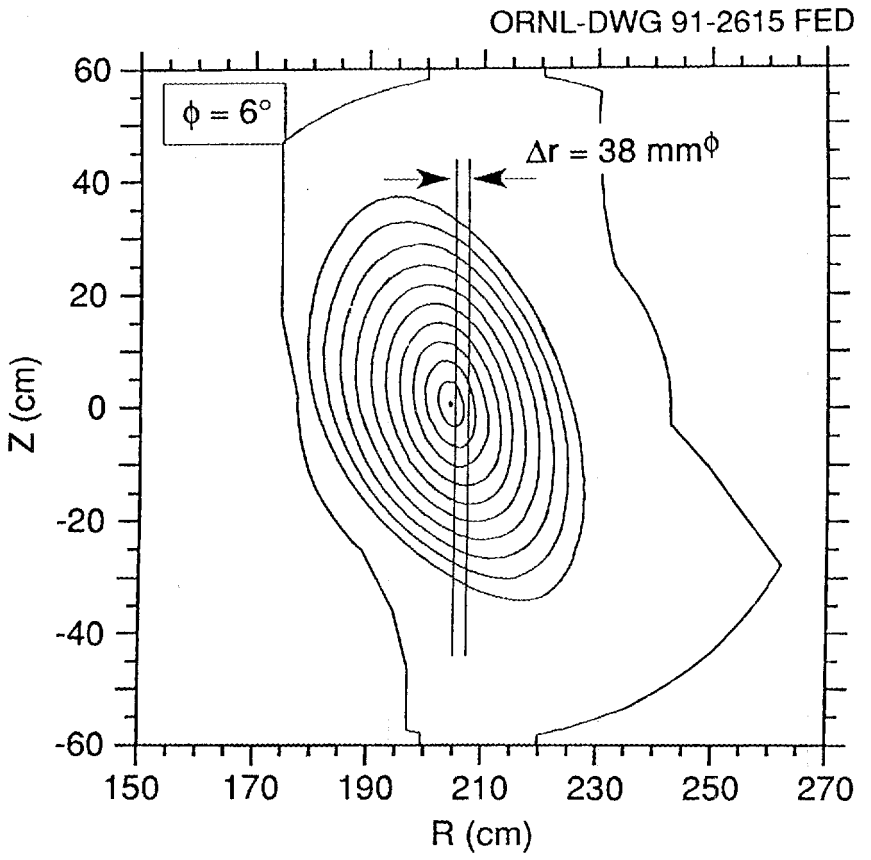

Fig. 7. Poloidal cross-section view of a typical ATF plasma and geometry of visible bremsstrahlung chord with a toroidal angle of $\phi = 6°$.

plasma cross section because electron and impurity density profiles [7] are flat over much of the plasma radius, and, as already discussed, the temperature dependence of the visible bremsstrahlung is weak.

The transmission characteristics of the interference filters are shown in Fig. 8. The bandwidth is centered at 6324 Å, where the peak transmission is 84%. The full width at half-maximum (FWHM) is 101 Å.

The plasma spectrum in the region of transmission of the filters was investigated in detail to make sure that no strong spectral lines were present, since they could lead to false interpretations of the magnitude of the visible bremsstrahlung signal. An optical multichannel analyzer (OMA) and visible spectrometer (McPherson model 2051) were used to investigate both ECH and NBI plasmas. The results are shown in Figs. 9–13. Figures 9 and 10 illustrate the spectra around 6324 Å from NBI plasmas without titanium gettering. The solid arrows indicate second-order spectral lines,

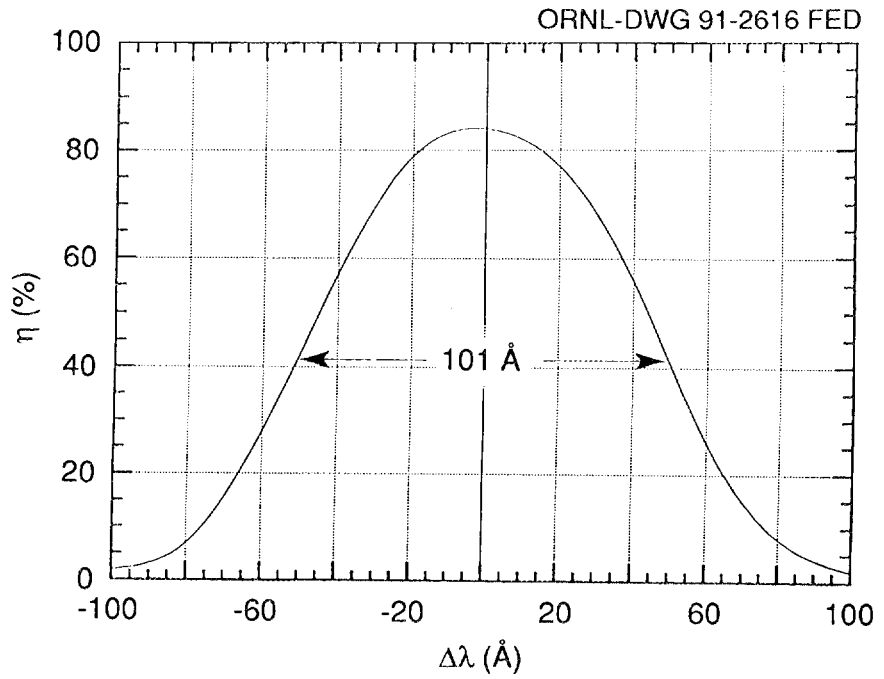

Fig. 8. Transmission rate η of the interference filter. The full width at half-maximum of the transmission curve is 101 Å, and the wavelength at the peak transmission rate is 6324 Å.

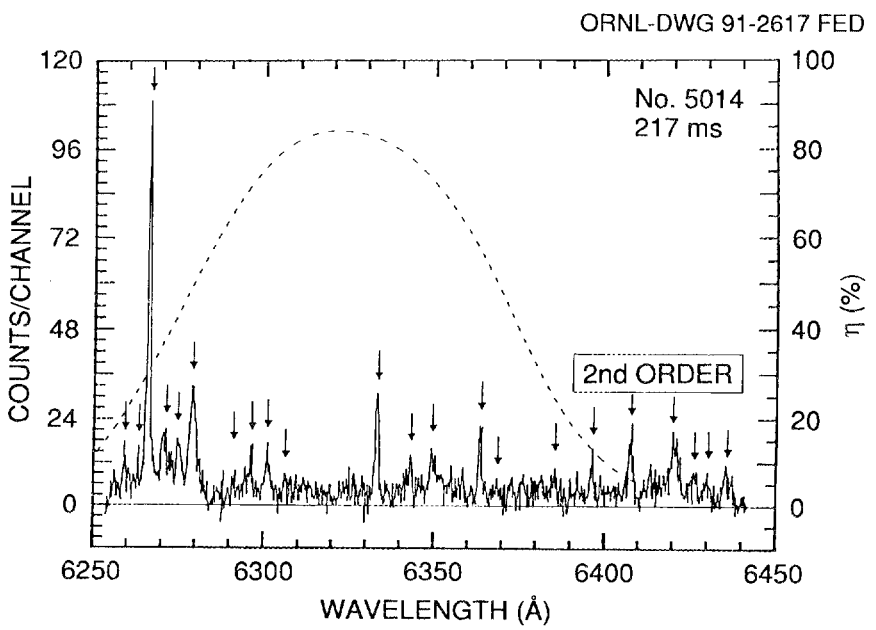

Fig. 9. Visible spectrum near 6324 Å at the middle of NBI pulse before gettering was initiated. The dotted curve indicates the transmission of the interference filter. Solid arrows indicate second-order light.

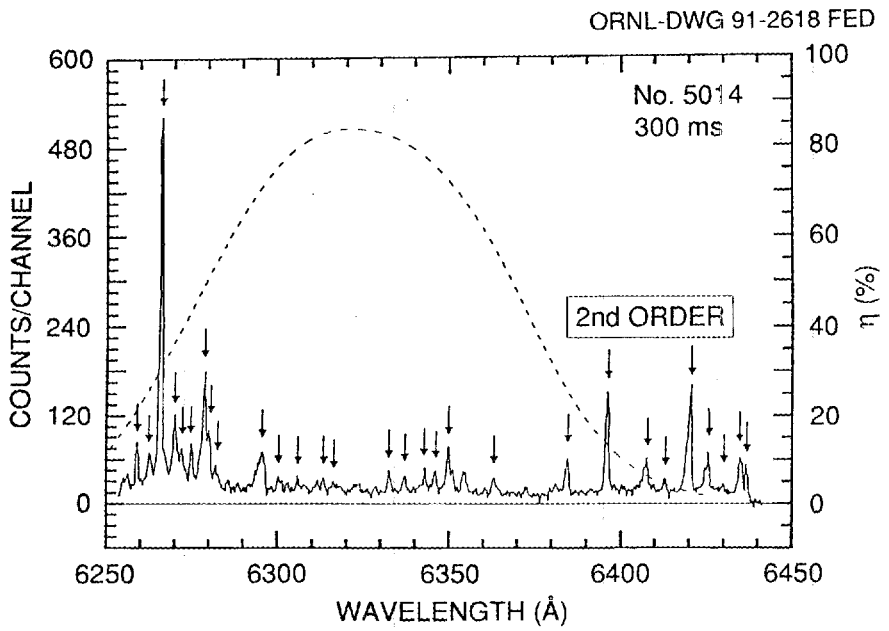

Fig. 10. Visible spectrum near 6324 Å at the end of NBI pulse, as in Fig. 9.

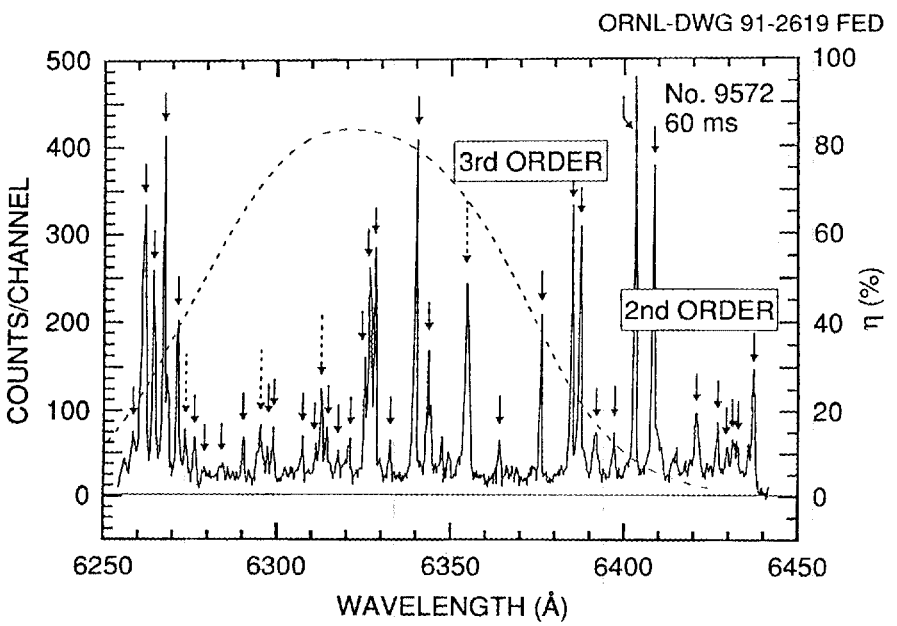

Fig. 11. Visible spectrum near 6324 Å at the beginning of ECH pulse after titanium gettering. Dashed arrows indicate third-order light.

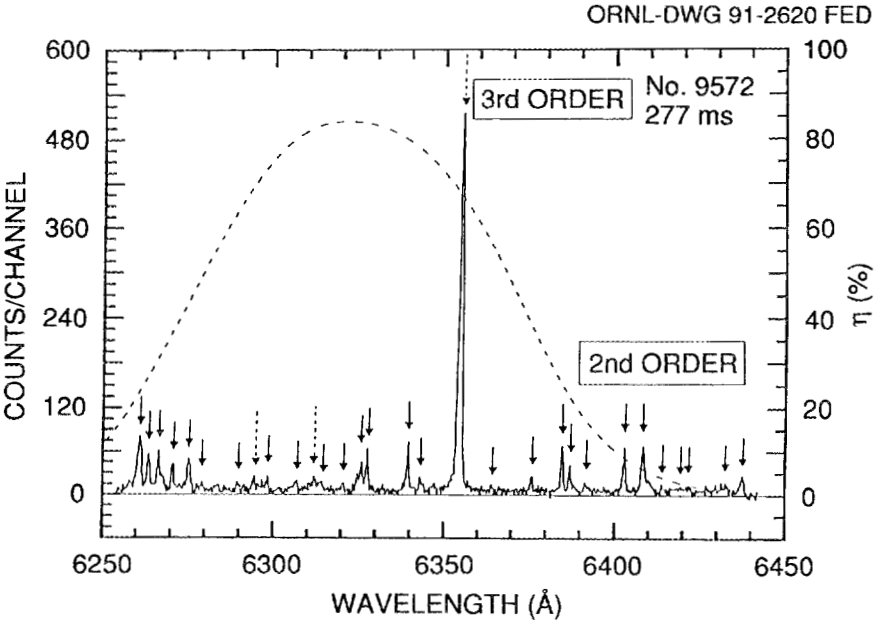

Fig. 12. Visible spectrum near 6324 Å at the middle of an ECH pulse.

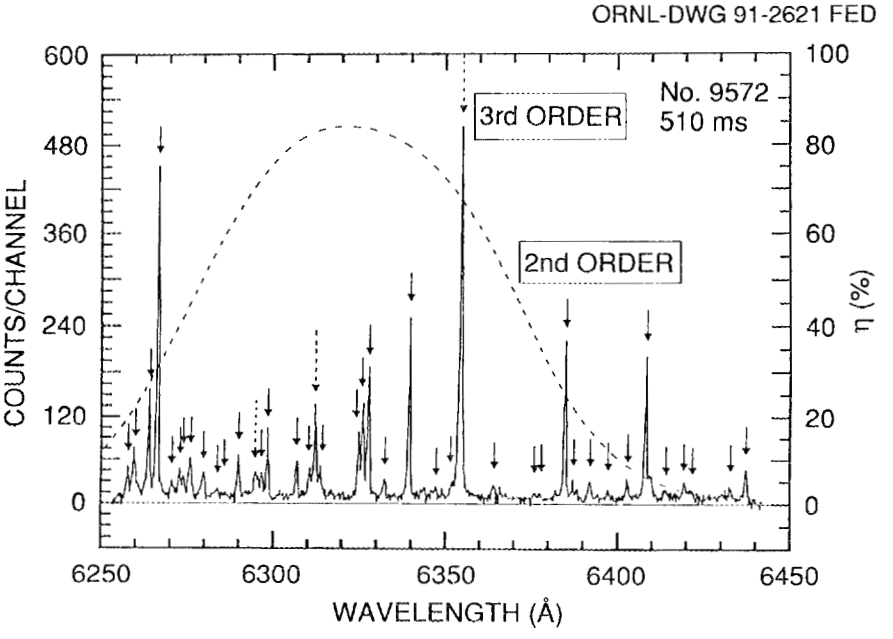

Fig. 13. Visible spectrum near 6324 Å at the end of an ECH pulse.

and the dotted curve is the transmission curve for the interference filter. All of the lines observed in this region appear to be second-order lines from carbon and oxygen, which are not transmitted by the filter; no first-order lines that could be transmitted by the filter are distinguishable.

Visible spectra from ECH plasmas after titanium gettering are shown in Figs. 11–13. The spectrum is dominated by titanium lines, which are prominent at the beginning (Fig. 11) and the end (Fig. 13) of the discharges. As designated by the arrows, most of these lines are again of higher order. Nevertheless, the radiation during the beginning and end of the discharges is not analyzed to obtain Z_{eff} even though the contribution from spectral lines is a small part of the signal. The analyses are carried out only for the interval of the discharge when all line intensities are weak except for the feature at 6354 Å (Fig. 12). The strong line at 6354 Å is believed to be the third order of the Ti XIV forbidden line at 2117.1 Å, which is not transmitted by the filter. Its time behavior is shown in Fig. 14. This history differs from that of an impurity line from a low ionization stage; it is similar to that of a highly ionized ion. Further support for our identification of this line is that its half-width is relatively broad, an indication that the emission originates from the center rather than the edge of the plasmas.

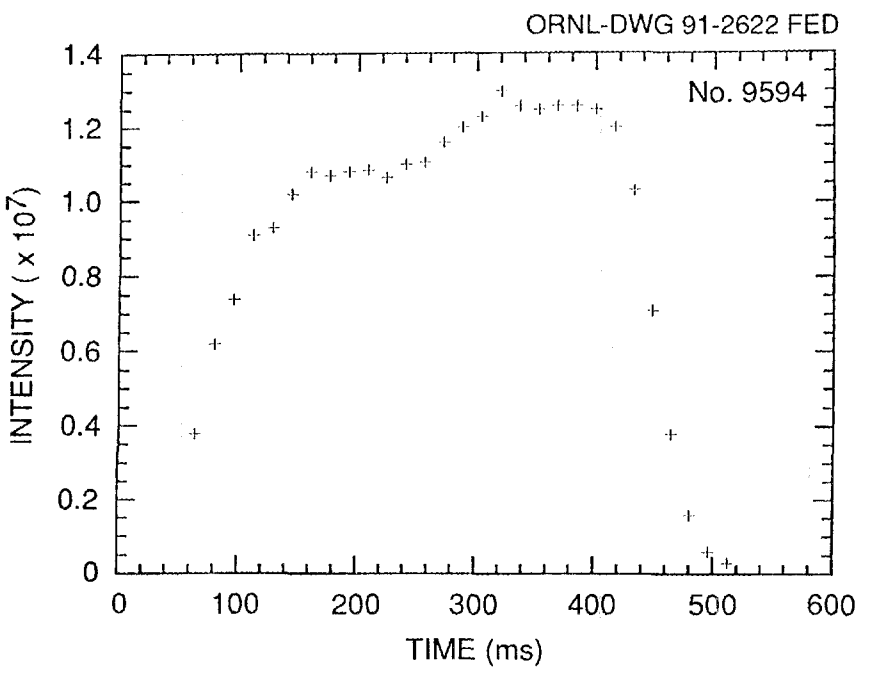

Fig. 14. Time behavior of Ti XIV forbidden line (third-order light) located at 6354 Å. The signal is characteristic of light from a highly ionized ion.

4. EXPERIMENTAL RESULTS AND DISCUSSION

In order to determine Z_{eff} from the visible bremsstrahlung, it is necessary to know the electron temperature [Eq. (4)]. Electron cyclotron emission (ECE) potentially provides a continuous measurement of T_e in ATF; however, the cutoff density at 1 T, which is the magnetic field usually employed, is only 2×10^{13} cm^{-3}, whereas the electron density is greater than this value for many types of operation. Therefore, an average electron temperature is deduced from a combination of the stored energy W_p as determined by the diamagnetic or saddle coil signals and the line-averaged electron density from the 2-mm interferometer:

$$\overline{T}_e = \frac{10^3 W_p}{(1.6 \times 10^{-19})\overline{n}_e V} \left(\frac{W_e}{W_p}\right), \tag{8}$$

where W_e represents the energy stored in the electrons alone. For $\overline{n}_e$ in particles per cubic centimeter and the plasma volume V in cubic centimeters (3.02×10^6 cm^3), the electron temperature is given in electron volts. The ratio W_e/W_p has been inferred to satisfy the following relation by comparing Thomson scattering measurements of T_e and n_e to the total stored energy given by the diamagnetic or saddle loops:

$$\frac{W_e}{W_p} = 0.5 + \frac{0.7}{n_e \ell} - \frac{0.2}{(n_e \ell)^2}. \tag{9}$$

This ratio is plotted in Fig. 15. The curve is normalized to unity for $n_e \ell = 10^{14}$ cm^{-2} ($\ell = 66$ cm, $\overline{n}_e = 1.5 \times 10^{12}$ cm^{-3}), although it is not realistic to assume that the ion temperature is zero at this density. This assumption presents no problem, since Z_{eff} measurements are always made well above this density. Nonetheless, it must be emphasized that Eq. (8) may not apply under all circumstances, particularly when the electron temperature changes rapidly.

By combining Eqs. (4), (5), (7), and (8) we get the following expressions for Z_{eff}:

$$Z_{\text{eff}} = 9.48 \times 10^3 S \left[W_p \left(0.5 + \frac{0.7}{n_e \ell} - \frac{0.2}{(n_e \ell)^2} \right) \right]^{0.35} (n_e \ell)^{-2.35} \tag{10}$$

or

$$Z_{\text{eff}} = 3.82 \times 10^{-11} I \left[W_p \left(0.5 + \frac{0.7}{n_e \ell} - \frac{0.2}{(n_e \ell)^2} \right) \right]^{0.35} (n_e \ell)^{-2.35}, \tag{11}$$

where $n_e \ell$ is the line-integrated interferometer signal in units of 10^{14} cm^{-2}, W_p is expressed in kilojoules, S (in volts) is the raw data signal from the visible

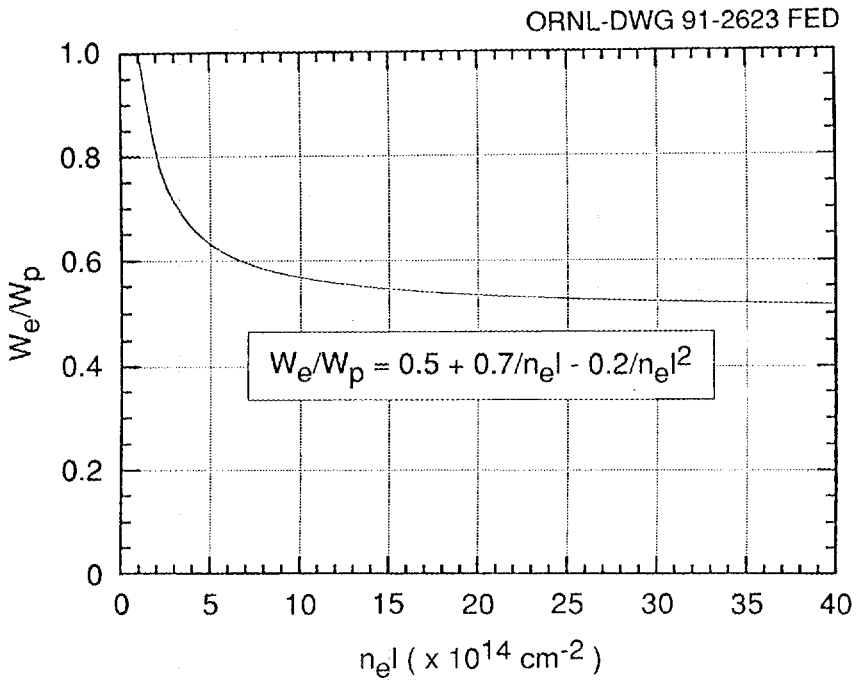

Fig. 15. Ratio of the electron stored energy to the plasma stored energy [Eq. (9)] as a function of line-integrated electron density.

bremsstrahlung system (ATF signal name: Vbrem_02), and I is the signal intensity expressed in photons/cm^2·s.

Various monitor signals of a typical ATF plasma with NBI are shown in Fig. 16. Neutral injection begins at 260 ms and lasts for 200 ms. The central electron temperature decreases from 1 keV in the ECH target plasma to 200–300 eV at 300 ms. The stored energy W_p from the saddle loops indicates an increase from 3 to 6 kJ after a sudden decrease of the gas puff at 370 ms. The visible bremsstrahlung signal exhibits a time behavior similar to that of the electron density until the stored energy begins to decrease around 410 ms.

The evolution of $Z_{\text{eff}}(0)$ obtained from this discharge is shown in Fig. 17. The increase from 200 to 235 ms is related to a decreasing electron density and a rising electron temperature [see Eq. (4)]. The visible bremsstrahlung signal itself does not change in this interval. The subsequent drop in the value of Z_{eff} between 240 and 260 ms results from a rise of the electron density as the gas puffing rate is rapidly increased when NBI begins. The following growth of the Z_{eff} value between 260 and 280 ms originates from an impurity influx. The buildup of the electron density and stabilization of the impurity concentration during NBI then lead to steady decline of Z_{eff} over the next 120 ms.

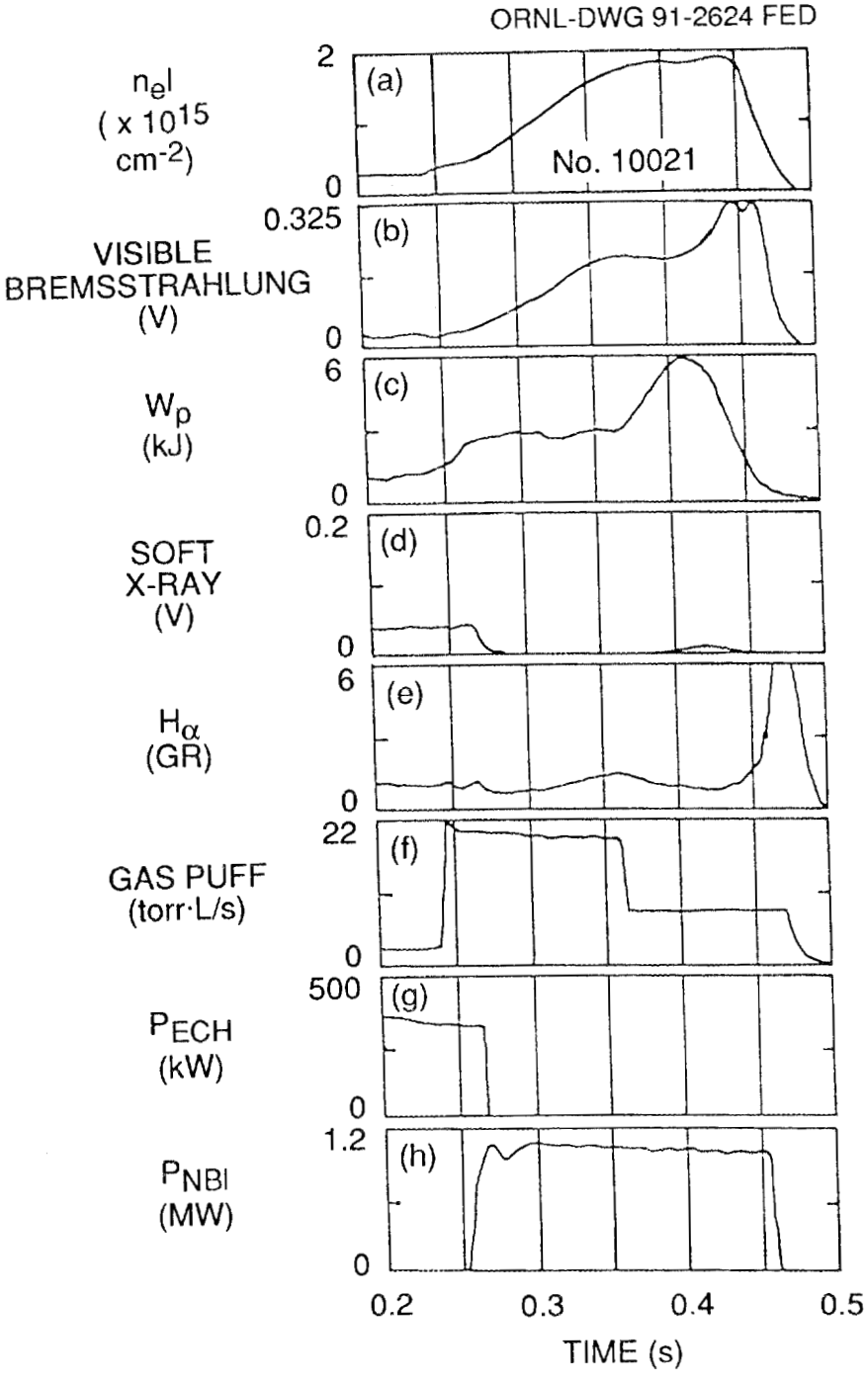

Fig. 16. Time behavior of (a) line-integrated electron density, (b) raw signal of visible bremsstrahlung, (c) plasma stored energy, (d) soft X-ray signal, (e) H_α intensity, (f) gas puffing rate, (g) ECH power, and (h) NBI power in a typical NBI plasma with a magnetic field of 1 T. The discharge exhibits a radiation collapse at the end of the NBI pulse.

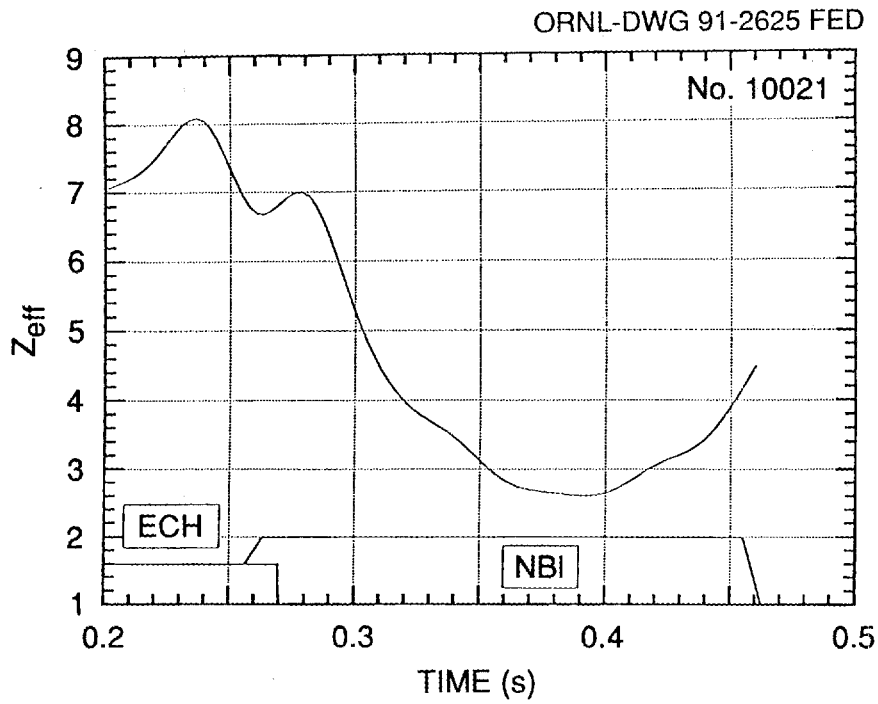

Fig. 17. Time behavior of Z_{eff} in the discharge of Fig. 16.

Some insight into the impurity behavior, as opposed to that of Z_{eff}, can be obtained by plotting $(Z_{\text{eff}} - 1)n_e\ell$ as a function of time, as shown in Fig. 18. If it is assumed that a single impurity is dominant in the discharge, Eq. (3) provides the relationship

$$\sum_i Z_i(Z_i - 1)n_i = (Z_{\text{eff}} - 1)n_e \ , \tag{12}$$

where the summation extends only over the ionization stages of that single impurity. We rewrite Eq. (12) as

$$(\overline{Q^2} - \overline{Q})n_{\text{imp}} = (Z_{\text{eff}} - 1)n_e \ , \tag{13}$$

where $\overline{Q}$ is the average impurity charge defined in Eq. (6). A plot of the right-hand side of Eq. (13) as a function of time is proportional to the history of the impurity concentration, provided the average impurity charge remains the same. However, because the temperature varies during the discharge, $\overline{Q}$ and $\overline{Q^2}$ do not remain constant, and Fig. 18 does not exactly represent the impurity evolution. Following the beginning of NBI at 250 ms, the plotted data indicate that the central impurity density rises by about 50% from 250 to 300 ms. Since the electron temperature falls from 1 keV to about 300 eV at 300 ms, $\overline{Q}$ should also decrease, so the fractional

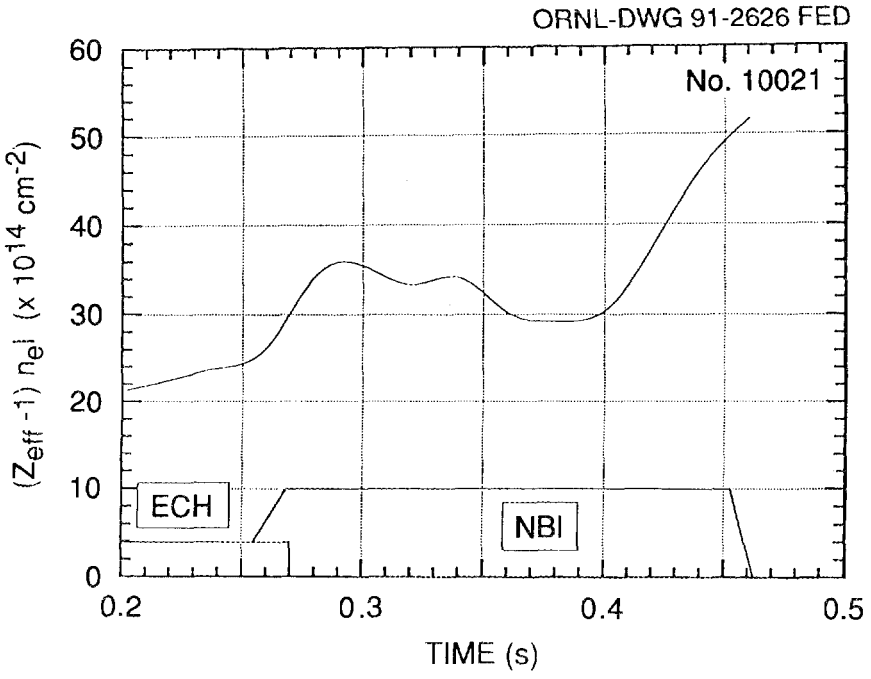

Fig. 18. Time behavior of the impurity amount denoted by $(Z_{\text{eff}} - 1)n_e\ell$. This graph shows clearly that the impurity amount increases at the onset of NBI.

change in the central impurity content after injection is actually greater than that inferred from Fig. 18. Typical analysis of spectroscopic data indicates increases in the impurity density of approximately a factor of two. In the period from 360 ms to 410 ms when the stored energy increases following a decline of the gas puffing rate, Fig. 18 indicates that the impurity level also begins to rise, at least from 390 ms onward. This behavior may imply that an increasing impurity content has some influence on initiating the collapse. However, note that when the stored energy reaches a maximum at 410 ms, the impurity level surmised from Fig. 18 is lower than in the interval from 290 to 340 ms, when the stored energy has a quasi-steady level at about one-half the peak value. After 390 ms, when the plasma temperature and density decay rapidly, analysis of the bremsstrahlung signal becomes less certain than at earlier times. It appears that radial profiles of the bremsstrahlung signal, as well as more accurate measurements of $T_e(r)$ and $n_e(r)$, will be necessary to obtain a precise interpretation of the impurity behavior.

The amplitudes of the visible bremsstrahlung signals (in millivolts) are plotted in Fig. 19 as a function of line-integrated electron density. The magnitude of the signals is generally smaller at lower electron densities. Below $n_e\ell \approx 10^{14}$ cm^{-2}, the

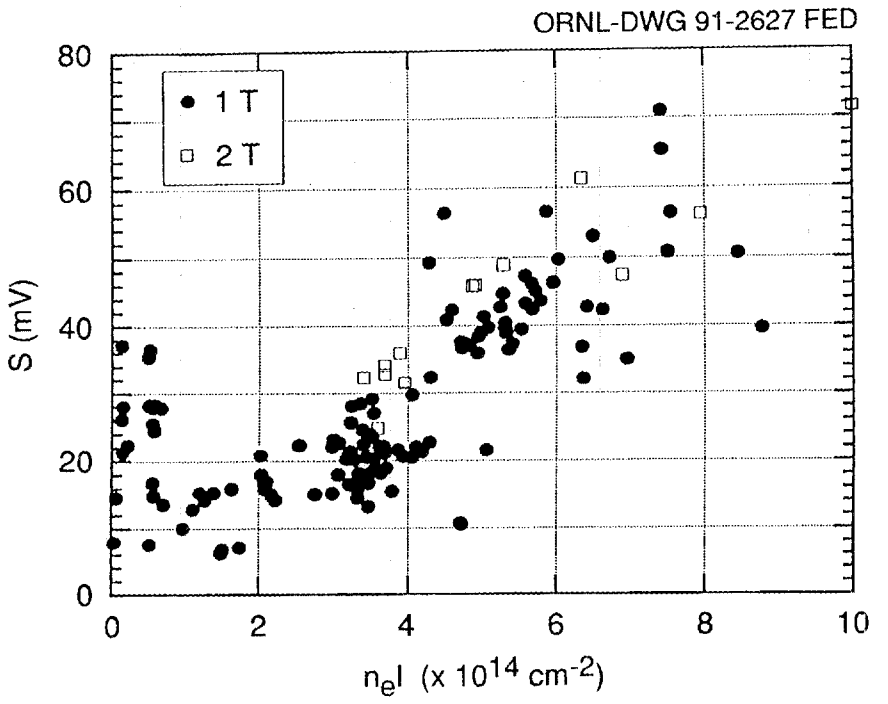

Fig. 19. Raw signals of visible bremsstrahlung in ECH plasmas as a function of line-integrated electron density. These signals have some offset, and they increase strongly at line-integrated densities less than 1×10^{14} cm^{-2}. The typical path length of plasma sampled by the 2-mm microwave interferometer is 60 cm.

minimum signals do not actually go to zero as expected but seem to have a baseline value of about 12 mV.

In order to investigate whether this baseline signal is peculiar to the wavelength region around 6324 Å, three additional detectors employing filters for different spectral regions were installed. The lines of sight of all three pass through the center of the vacuum chamber. Results from low-density ECH plasmas are summarized in Table 1. A nonzero baseline signal is observed in all channels. These results indicate that some source of radiation, such as weak spectral line emissions or nonthermal electrons, is responsible for the baseline signal. The values of Z_{eff} calculated without subtracting the baseline are shown in Fig. 20; they reach values as high as 16 for $n_e\ell = 3 \times 10^{14}$ cm^{-2}. Figure 21 shows the more accurate values of Z_{eff} calculated by subtracting a baseline of 12 mV from the raw data. The large variation at any given density results from variations in wall condition, electron temperatures, magnetic configuration, and existence of plasma collapses. The impurity density reflected by $(Z_{\text{eff}} - 1)n_e\ell$ as a function of electron density is shown in Fig. 22. Clearly, the spread

Table 1. Comparison of visible bremsstrahlung signals from different filters at 200 ms in a 1-T ECH plasma (shot 10876)

	ATF signal name			
	Vbrem_02	Vbrem_06	Vbrem_03	Vbrem_04
Wavelength λ_0,Å	6328	7668	8387	9008
FWHM $\Delta\lambda$,Å	101	103	114	143
Signal, mV	20.0	8.0	8.0	2.0
Z_{eff}	19.8	40.0	32.9	17.4

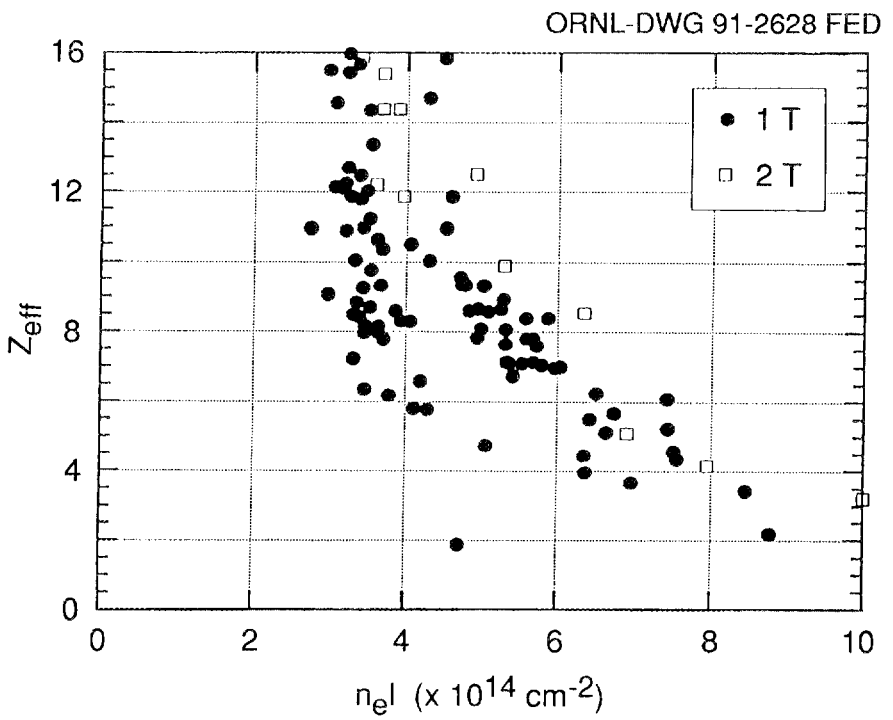

Fig. 20. Z_{eff} obtained directly from the raw signals shown in Fig. 19 as a function of line-integrated electron density.

in the data points is large, but above $n_e\ell = 4 \times 10^{14}$ cm^{-2} the impurity densities tend to decrease with increasing electron densities. There is no clear difference between operation at 1 T and operation at 2 T.

When analyzing the NBI interval of a discharge with relatively high density, the baseline signal presents little problem since the visible bremsstrahlung radiation is

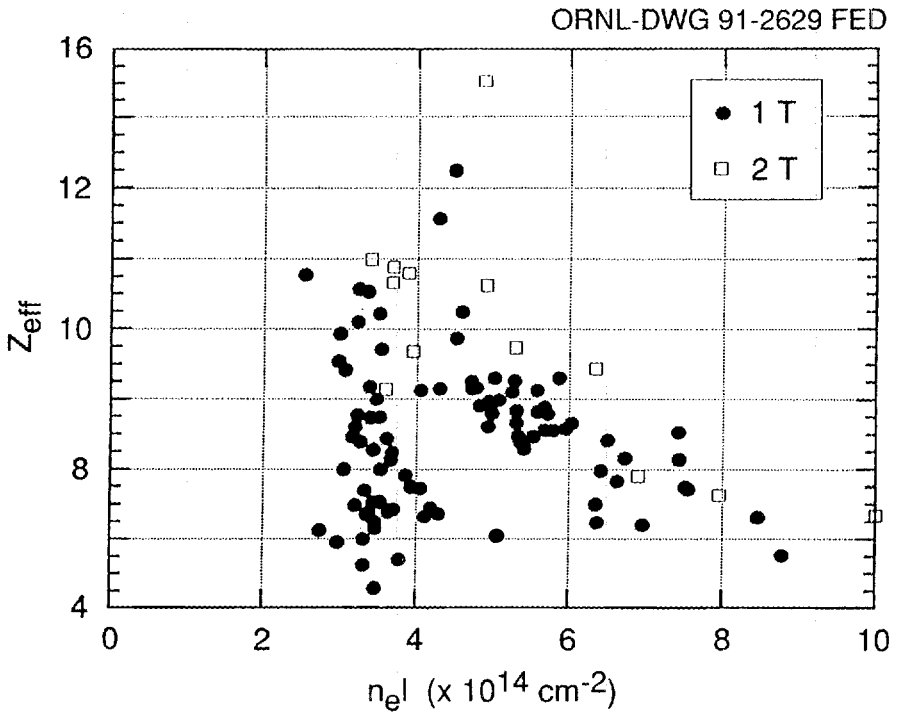

Fig. 21. Z_{eff} obtained by subtracting 12 mV from the raw signals as a function of line-integrated electron density.

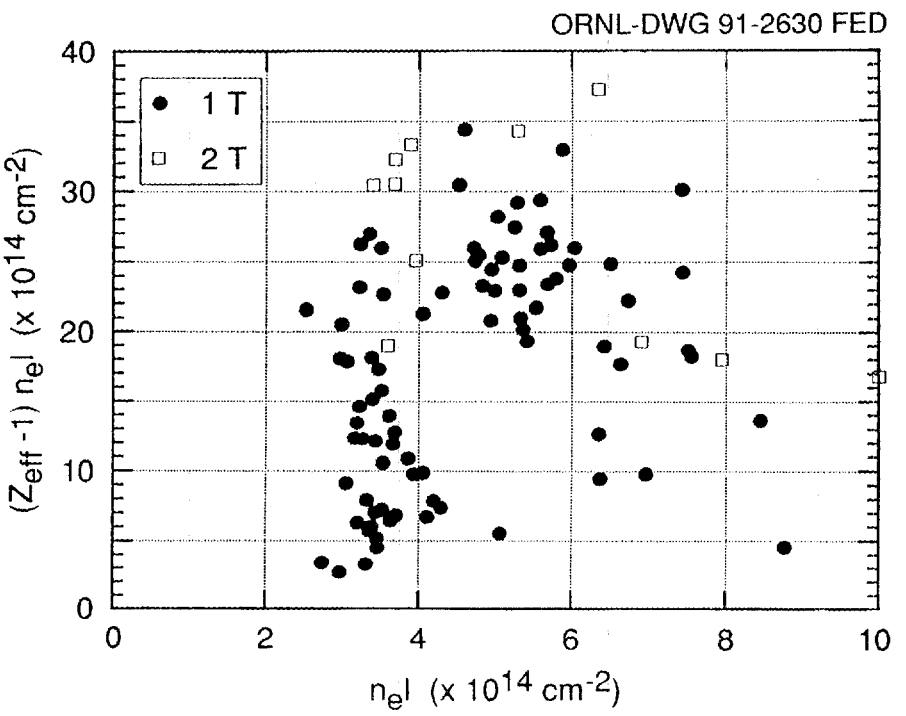

Fig. 22. Impurity amount denoted by $(Z_{\mathrm{eff}} - 1)n_e\ell$ in the ECH plasmas as a function of line-integrated electron density.

much stronger. The magnitude of the signals from NBI plasmas is illustrated in Fig. 23, and the values of Z_{eff} for these plasmas are shown in Fig. 24. The magnitude of Z_{eff} becomes relatively large below $n_e\ell = 2 \times 10^{15}$ cm^{-2}. NBI discharges in this low-density region generally collapse. Plasmas produced at 2 T also tend to collapse when the line-integrated density is around 4×10^{15} cm^{-2}. In general, Z_{eff} appears to be higher for both 1 and 2 T in plasmas which collapse than in those which do not, but this may be an artifact connected with the rapidly dropping electron temperatures and unusually large signals from marfes, which have been observed at the time of stored energy peaking. In the steady-state interval of both 1- and 2-T plasmas that do not collapse, Z_{eff} is usually less than 2.5.

The values of $(Z_{\text{eff}} - 1)n_e\ell$ are shown in Fig. 25 for NBI discharges. The scatter of data points at any given density is very large, and the smaller values are generally indicative of discharges that do not collapse. If it is assumed that titanium is the dominant impurity in the plasma and that the average charge $\overline{Q}$ at the plasma center is 15, the concentration of titanium is computed to be 0.35% during 1-T operation and 0.11% during 2-T operation.

The radial profiles of $\overline{Q}$ calculated for 1% oxygen and 1% titanium concentrations are shown in Figs. 26 and 27. The profiles of electron temperature and density are the same as those used for Figs. 3–6. Central electron temperatures of 0.8 eV and 0.2 eV are assumed for central electron densities of 10^{13} cm^{-3} and 10^{14} cm^{-3}. The $\overline{Q}$ profiles are relatively flat because the ionization balance does not change appreciably inside $0.9\overline{a}_p$. As a result, the Z_{eff} profiles (Figs. 28 and 29) are also relatively flat except for the rapid decrease outside $0.8\overline{a}_p$.

At present, radial profiles of Z_{eff} are not measured in ATF. However, the calculated profiles shown in Figs. 28 and 29 indicate that it may be worthwhile to measure the Z_{eff} profile in detail beyond $0.8\overline{a}_p$.

5. SUMMARY

Measurements of Z_{eff} for both ECH and NBI plasmas have been carried out using visible bremsstrahlung radiation. In order to obtain continuous electron temperature measurements during the discharges, which are needed to obtain Z_{eff} from the bremsstrahlung measurements, the plasma stored energy and electron density are used. In very low density ECH plasmas it is clear that a baseline level

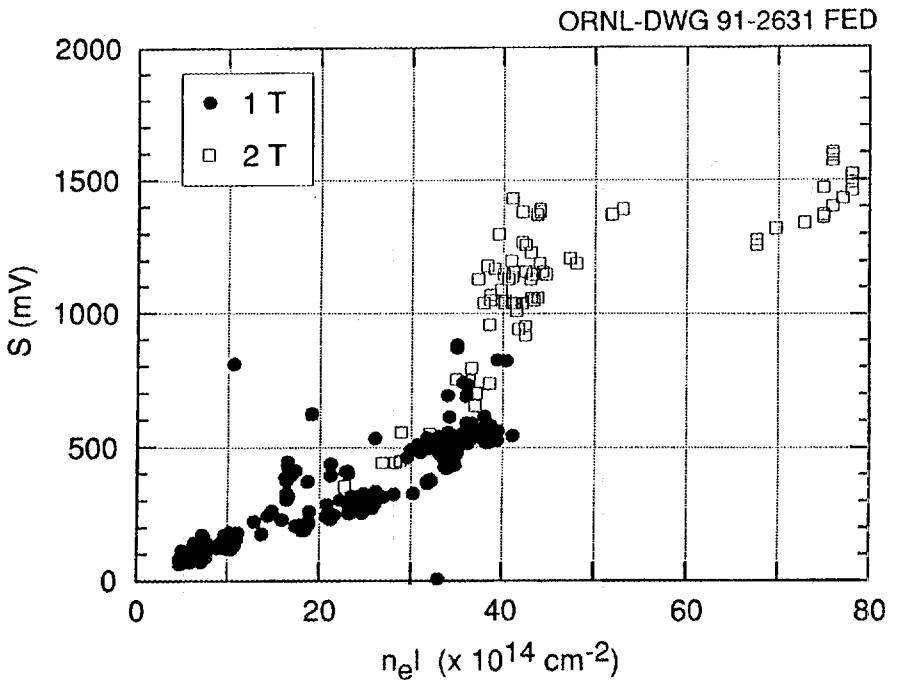

Fig. 23. Raw signals of visible bremsstrahlung in NBI plasmas as a function of line-integrated electron density.

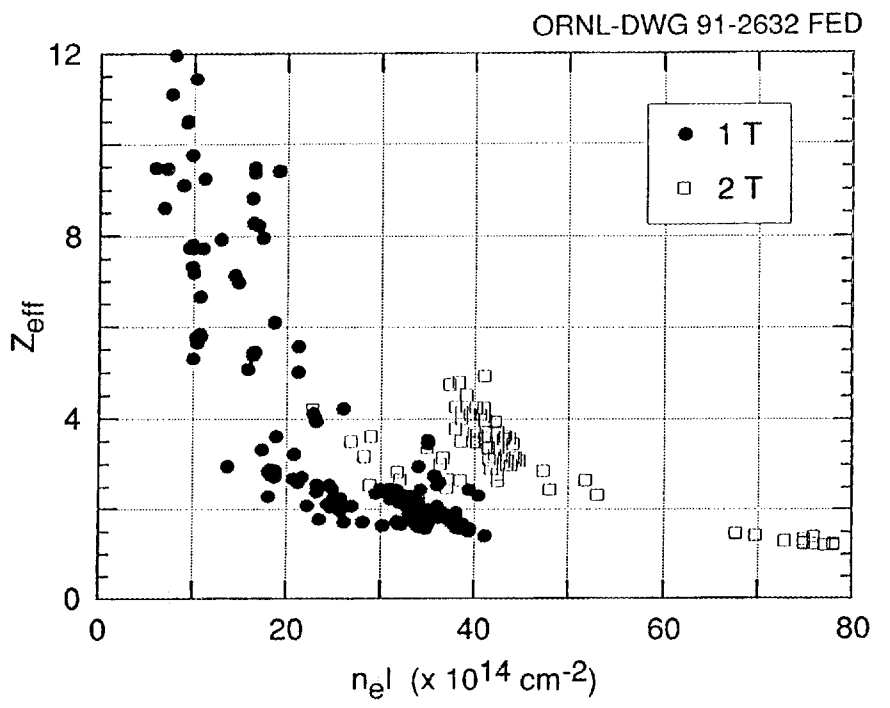

Fig. 24. Z_{eff} in NBI plasmas as a function of line-integrated electron density. NBI discharges with Z_{eff} larger than 3 are accompanied by radiation collapse.

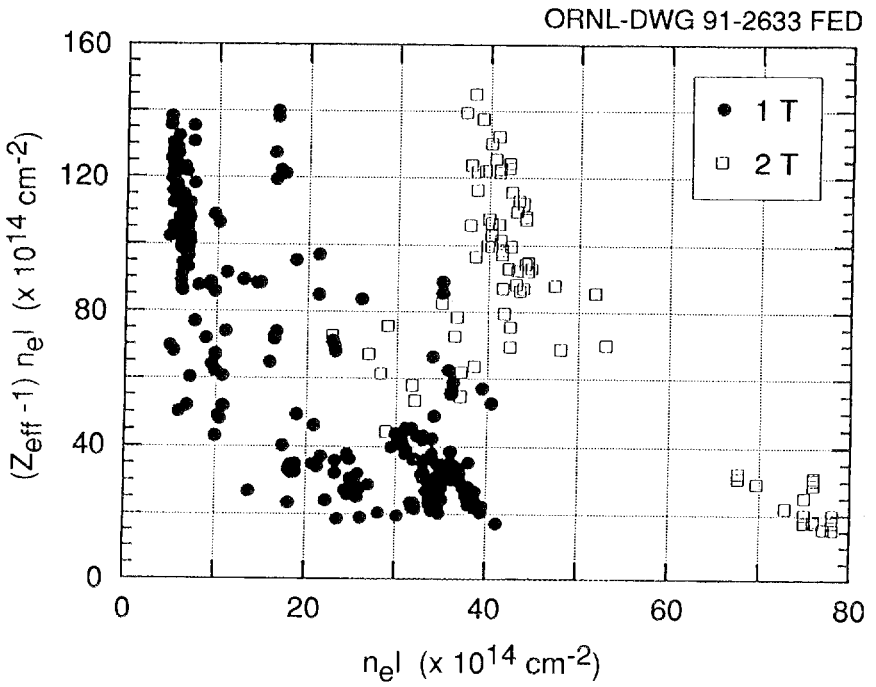

Fig. 25. Impurity amount denoted by $(Z_{\text{eff}} - 1)n_e\ell$ in NBI plasma as a function of line-integrated electron density.

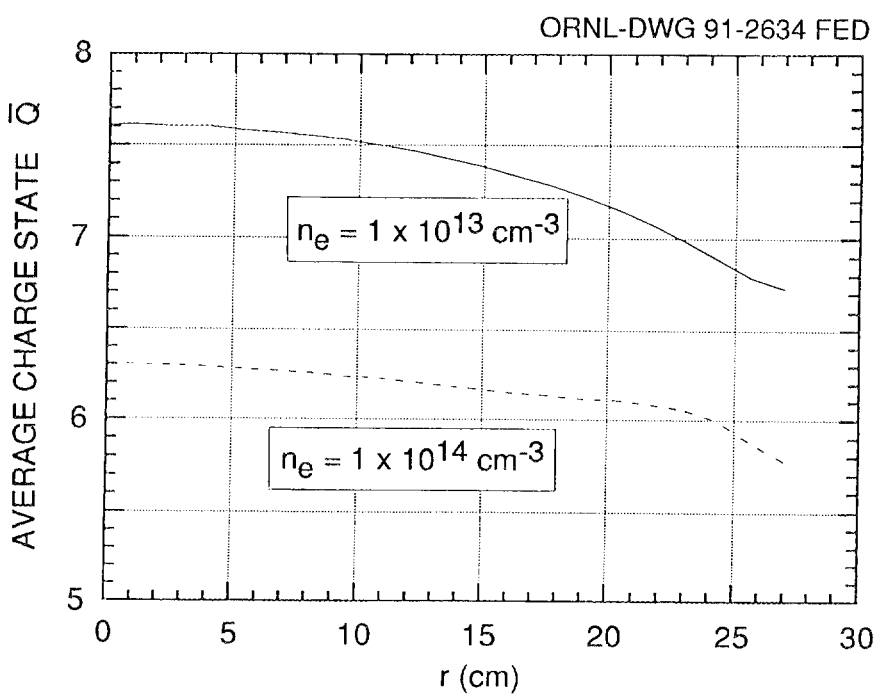

Fig. 26. Calculations of radial profiles of average charge state $\overline{Q}$ for oxygen. Electron temperatures of 0.8 keV and 0.2 keV are given in the calculations at the central electron densities of $n_e = 1 \times 10^{13}$ cm^{-3} and 1×10^{14} cm^{-3}, respectively. Other parameters are the same as in Figs. 3–6.

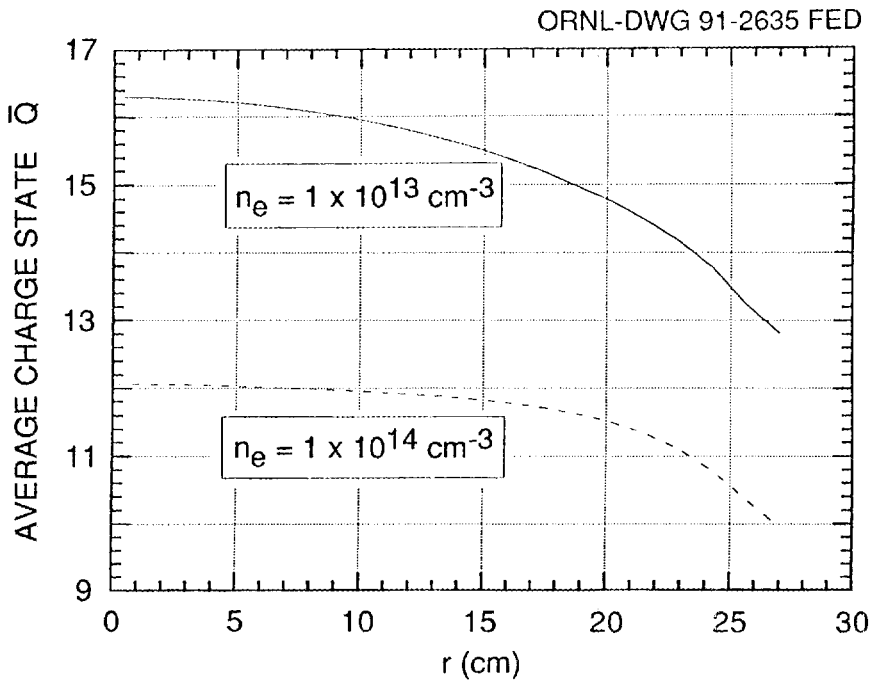

Fig. 27. Calculations of radial profiles of average charge state $\overline{Q}$ for titanium.

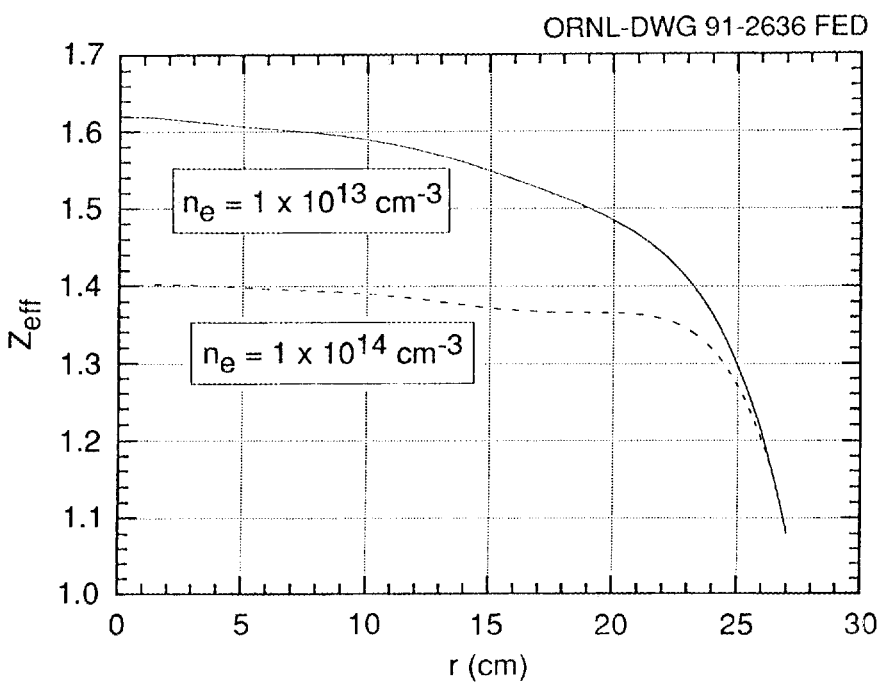

Fig. 28. Calculations of radial profiles of Z_{eff} for 1% oxygen.

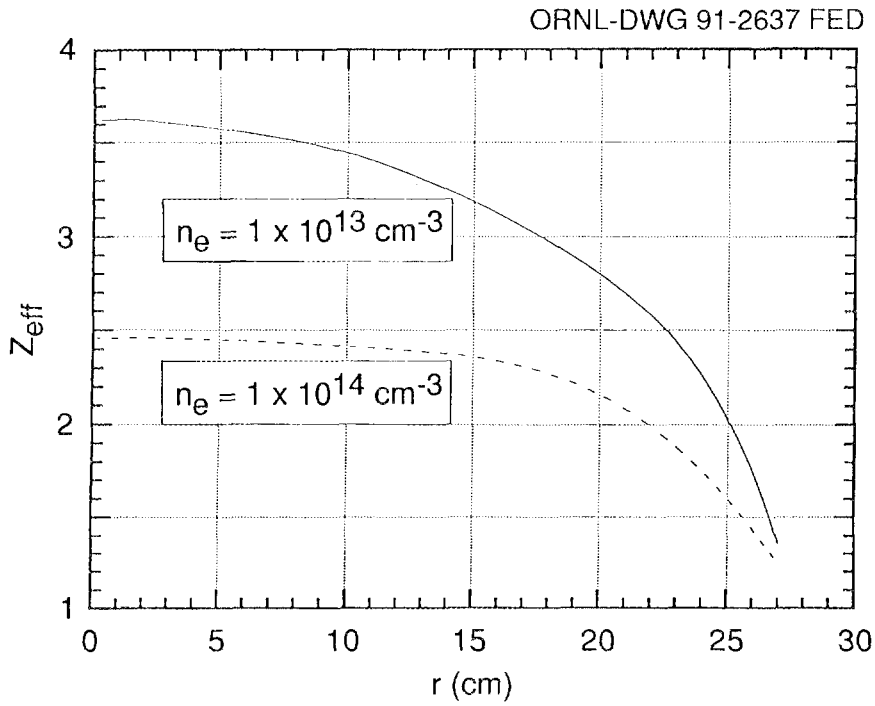

Fig. 29. Calculations of radial profiles of Z_{eff} for 1% titanium.

of radiation appears in the detection system and does not originate from visible bremsstrahlung. This baseline adds some uncertainty at low densities to the measured values of Z_{eff}, which are between 2 and 8 depending on the experimental conditions.

In NBI plasmas the values depend strongly on the existence of radiation collapse. In plasmas that undergo radiation collapse the Z_{eff} values are between 3 and 5 when the stored energy reaches a transient maximum. However, in quasi-steady plasmas without collapse Z_{eff} is less than 2.5, and in very high density plasmas, $n_e\ell \approx 7.5 \times 10^{15}$ cm^{-2}, Z_{eff} is close to 1.2.

ACKNOWLEDGMENT

This work was carried out as part of a collaboration (QL81) between the Ministry of Education in Japan and the Department of Energy in the United States. The authors thank all the members of the ATF group for their cooperation in carrying out this research and for valuable discussions concerning diagnostic results. The authors also are grateful for the encouragement of J. L. Dunlap, J. F. Lyon, J. Sheffield (director of the ORNL Fusion Energy Division), K. Matsuoka, and A. Iiyoshi (director of the National Institute for Fusion Science, Japan).

REFERENCES

1. R. C. Isler et al., "Impurity Studies in the Advanced Toroidal Facility," p. 619 in *Controlled Fusion and Plasma Physics: Proceedings of the 16th European Conference, Venice, 1989,* Vol. 13B, Pt. II, European Physical Society, Petit-Lancy, Switzerland, 1989.

2. H. Ringler et al., "Impurity Behaviour in the Wendelstein VII-A Stellarator," pp. 603–613 in *Plasma Physics and Controlled Nuclear Fusion Research: Proceedings of the 11th International Conference, Kyoto, 1986,* Vol. 2, International Atomic Energy Agency, Vienna, 1987.

3. K. Kondo et al., *Jpn. J. Appl. Phys.* **27**, 2368 (1988).

4. K. Kadota, M. Otsuka, and J. Fujita, *Nucl. Fusion* **20**, 209 (1980).

5. K. Ida et al., *Nucl. Fusion* **30**, 665 (1990).

6. S. Morita and CHS Group, p. 228 in *Proceedings of the First International Toki Conference on Plasma Physics and Controlled Fusion,* NIFS-PROC-3, National Institute of Fusion Science, Nagoya, Japan, 1990.

7. R. C. Isler et al., "Spectroscopic Studies of Plasma Collapse in the Advanced Toroidal Facility," *Nucl. Fusion* **29**, 1384–90 (1989).

8. R. C. Isler et al., "Cleanup and Improvement of Operational Performance of ATF by Chromium and Titanium Gettering," pp. 455–8 in *Controlled Fusion and Plasma Physics: Proceedings of the 17th European Conference, Amsterdam, 1990,* Vol. 14B, European Physical Society, Petit-Lancy, Switzerland, 1990.

9. W. Finkelnburg and T. Peters, *Handbüch der Physik* **28**, 79 (1957).

10. W. J. Karzas and R. Latter, *Astrophys. J. Suppl.* **55**, 167 (1961).

11. K. Matsuoka et al., p. 93 in *Proceedings of the First International Toki Conference on Plasma Physics and Controlled Fusion,* NIFS-PROC-3, National Institute of Fusion Science, Nagoya, Japan, 1990.

12. A. C. England and D. A. Rasmussen, Oak Ridge National Laboratory, personal communication, 1990.

ORNL/TM-11737
Dist. Category UC-426

INTERNAL DISTRIBUTION

1. Director, Fusion Energy Division
2. C. C. Baker
3. M. J. Saltmarsh
4. L. A. Berry
5. B. A. Carreras
6. R. A. Dory
7. J. L. Dunlap
8. H. H. Haselton
9. M. S. Lubell
10. T. E. Shannon

11–12. Laboratory Records Department
13. Laboratory Records, ORNL-RC
14–15. Central Research Library
16. Document Reference Section
17. Fusion Energy Division Library
18–19. ET/FE Division Publications Office
20. ORNL Patent Office
21–22. R. K. Richards
23–24. L. D. Horton
25–29. R. C. Isler
30–31. E. C. Crume, Jr.
32–33. M. Murakami
34. R. A. Phaneuf

EXTERNAL DISTRIBUTION

35–36. S. Morita, National Institute for Fusion Science, Chikusa-ku, Nagoya 464-01, Japan
37. Office of the Assistant Manager for Energy Research and Development, U.S. Department of Energy, Oak Ridge Operations Office, P.O. Box E, Oak Ridge, TN 37831
38. J. D. Callen, Department of Nuclear Engineering, University of Wisconsin, Madison, WI 53706-1687
39. R. W. Conn, Department of Chemical, Nuclear, and Thermal Engineering, University of California, Los Angeles, CA 90024
40. N. A. Davies, Acting Director, Office of Fusion Energy, Office of Energy Research, ER-50 Germantown, U.S. Department of Energy, Washington, DC 20545
41. S. O. Dean, Fusion Power Associates, Inc., 2 Professional Drive, Suite 248, Gaithersburg, MD 20879

42. H. K. Forsen, Bechtel Group, Inc., Research Engineering, P. O. Box 3965, San Francisco, CA 94119
43. R. W. Gould, Department of Applied Physics, California Institute of Technology, Pasadena, CA 91125
44. R. A. Gross, Plasma Research Laboratory, Columbia University, New York, NY 10027
45. D. M. Meade, Princeton Plasma Physics Laboratory, P.O. Box 451, Princeton, NJ 08543
46. M. Roberts, International Programs, Office of Fusion Energy, Office of Energy Research, ER-52 Germantown, U.S. Department of Energy, Washington, DC 20545
47. W. M. Stacey, School of Nuclear Engineering and Health Physics, Georgia Institute of Technology, Atlanta, GA 30332
48. D. Steiner, Nuclear Engineering Department, NES Building, Tibbetts Avenue, Rensselaer Polytechnic Institute, Troy, NY 12181
49. R. Varma, Physical Research Laboratory, Navrangpura, Ahmedabad 380009, India
50. Bibliothek, Max-Planck Institut für Plasmaphysik, Boltzmannstrasse 2, D-8046 Garching, Federal Republic of Germany
51. Bibliothek, Institut für Plasmaphysik, KFA Jülich GmbH, Postfach 1913, D-5170 Jülich, Federal Republic of Germany
52. Bibliothek, KfK Karlsruhe GmbH, Postfach 3640, D-7500 Karlsruhe 1, Federal Republic of Germany
53. Bibliotheque, Centre de Recherches en Physique des Plasmas, Ecole Polytechnique Fédérale de Lausanne, 21 Avenue des Bains, CH-1007 Lausanne, Switzerland
54. J. Tachon, CEN/Cadarache, Departement de Recherches sur la Fusion Contrôlée, F-13108 Saint-Paul-lez-Durance Cedex, France
55. Bibliothèque, CEN/Cadarache, F-13108 Saint-Paul-lez-Durance CEDEX, France
56. Library, AEA Fusion, Culham Laboratory, Abingdon, Oxon OX14 3DB, England
57. Library, JET Joint Undertaking, Abingdon, Oxon OX14 3EA, England
58. Library, FOM-Instituut voor Plasmafysica, Rijnhuizen, Edisonbaan 14, 3439 MN Nieuwegein, The Netherlands
59. Library, National Institute for Fusion Science, Chikusa-ku, Nagoya 464-01, Japan
60. Library, International Centre for Theoretical Physics, P.O. Box 586, I-34100 Trieste, Italy
61. Library, Centro Richerche Energia Frascati, C.P. 65, I-00044 Frascati (Roma), Italy
62. Library, Plasma Physics Laboratory, Kyoto University, Gokasho, Uji, Kyoto 611, Japan
63. Plasma Research Laboratory, Australian National University, P.O. Box 4, Canberra, A.C.T. 2601, Australia

64. Library, Japan Atomic Energy Research Institute, Naka Fusion Research Establishment, 801-1 Mukoyama, Naka-machi, Naka-gun, Ibaraki-ken, Japan
65. G. A. Eliseev, I. V. Kurchatov Institute of Atomic Energy, P.O. Box 3402, 123182 Moscow, U.S.S.R.
66. V. A. Glukhikh, Scientific-Research Institute of Electro-Physical Apparatus, 188631 Leningrad, U.S.S.R.
67. I. Shpigel, Institute of General Physics, U.S.S.R. Academy of Sciences, Ulitsa Vavilova 38, Moscow, U.S.S.R.
68. D. D. Ryutov, Institute of Nuclear Physics, Siberian Branch of the Academy of Sciences of the U.S.S.R., Sovetskaya St. 5, 630090 Novosibirsk, U.S.S.R.
69. O. Pavlichenko, Kharkov Physical-Technical Institute, Academical St. 1, 310108 Kharkov, U.S.S.R.
70. Deputy Director, Southwestern Institute of Physics, P.O. Box 15, Leshan, Sichuan, China (PRC)
71. Director, The Institute of Plasma Physics, P.O. Box 26, Hefei, Anhui, China (PRC)
72. R. A. Blanken, Experimental Plasma Research Branch, Division of Applied Plasma Physics, Office of Fusion Energy, Office of Energy Research, ER-542, Germantown, U.S. Department of Energy, Washington, DC 20545
73. R. A. E. Bolton, IREQ Hydro-Quebec Research Institute, 1800 Montee Ste.-Julie, Varennes, P.Q. JOL 2P0, Canada
74. D. H. Crandall, Director, Division of Applied Plasma Physics, Office of Fusion Energy, Office of Energy Research, ER-542, Germantown, U.S. Department of Energy, Washington, DC 20545
75. R. L. Freeman, General Atomics, P.O. Box 85608, San Diego, CA 92138-5608
76. R. F. Gandy, Physics Department, Auburn University, Auburn, AL 36849
77. K. W. Gentle, RLM 11.222, Institute for Fusion Studies, University of Texas, Austin, TX 78712
78. R. J. Goldston, Princeton Plasma Physics Laboratory, P.O. Box 451, Princeton, NJ 08543
79. J. C. Hosea, Princeton Plasma Physics Laboratory, P.O. Box 451, Princeton, NJ 08543
80. D. Markevich, Division of Applied Plasma Physics, Office of Fusion Energy, Office of Energy Research, ER-55, Germantown, U.S. Department of Energy, Washington, DC 20545
81. R. H. McKnight, Experimental Plasma Research Branch, Division of Applied Plasma Physics, Office of Fusion Energy, Office of Energy Research, ER-542, Germantown, U.S. Department of Energy, Washington, DC 20545
82. E. Oktay, Division of Confinement Systems, Office of Fusion Energy, Office of Energy Research, ER-55, Germantown, U.S. Department of Energy, Washington, DC 20545
83. D. Overskei, General Atomics, P.O. Box 85608, San Diego, CA 92138-5608
84. R. R. Parker, Plasma Fusion Center, NW 16-288, Massachusetts Institute of Technology, Cambridge, MA 02139

85. W. L. Sadowski, Fusion Theory and Computer Services Branch, Division of Applied Plasma Physics, Office of Fusion Energy, Office of Energy Research, ER-541, Germantown, U.S. Department of Energy, Washington, DC 20545
86. J. W. Willis, Division of Confinement Systems, Office of Fusion Energy, Office of Energy Research, ER-55, Germantown, U.S. Department of Energy, Washington, DC 20545
87. A. P. Navarro, Division de Fusion, CIEMAT, Avenida Complutense 22, E-28040 Madrid, Spain
88. Laboratory for Plasma and Fusion Studies, Department of Nuclear Engineering, Seoul National University, Shinrim-dong, Gwanak-ku, Seoul 151, Korea
89. J. L. Johnson, Plasma Physics Laboratory, Princeton University, P.O. Box 451, Princeton, NJ 08543
90. L. M. Kovrizhnykh, Institute of General Physics, U.S.S.R. Academy of Sciences, Ulitsa Vavilova 38, 117924 Moscow, U.S.S.R.
91. O. Motojima, National Institute for Fusion Science, Chikusa-ku, Nagoya 464-01, Japan
92. S. Okamura, Institute of Plasma Physics, Nagoya University, Chikusa-ku, Nagoya 464, Japan
93. V. D. Shafranov, I. V. Kurchatov Institute of Atomic Energy, P.O. Box 3402, 123182 Moscow, U.S.S.R.
94. J. L. Shohet, Torsatron/Stellarator Laboratory, University of Wisconsin, Madison, WI 53706
95. H. Wobig, Max-Planck Institut fur Plasmaphysik, D-8046 Garching, Federal Republic of Germany

96–148. Given distribution as shown in OSTI-4500, Magnetic Fusion Energy (Category Distribution UC-426, Experimental Plasma Physics)